Journal of Materials Chemistry A

RSC Publishing

PAPER

View Article Online
View Journal | View Issue

Cite this: J. Mater. Chem. A, 2013, 1, 10667

Supercritical-fluid synthesis of FeF_2 and CoF_2 Li-ion conversion materials

Mark J. Armstrong,[ab] Arunkumar Panneerselvam,[ab] Colm O'Regan,[ab] Michael A. Morris[ab] and Justin D. Holmes*[ab]

Received 21st June 2013
Accepted 22nd July 2013

DOI: 10.1039/c3ta12436c

www.rsc.org/MaterialsA

The synthesis of the Li-ion conversion candidates, FeF_2 and CoF_2, obtained from the single source organometallic precursors [Fe(tta)$_3$] (tta = $C_8H_4F_3O_2S$), and [Co(hfac)$_2$·2H$_2$O] (hfac = $C_5H_1F_6O_2$), respectively, *via* a novel supercritical fluid (SCF) method is presented. The nature of the synthesis led to highly-crystalline FeF_2 and CoF_2 powders requiring no additional thermal treatment. The as-obtained powders were investigated for use as potential positive Li-ion conversion electrodes by means of chronopotentiometric measurements. The FeF_2 cells displayed high initial capacities following electrochemical conversion (up to ~1100 mA h g^{-1} at a potential of 1.0 V *vs.* Li/Li$^+$), with appreciable cyclic behaviour over 25 discharge–charge cycles. The deposition of a ~5 nm layer of amorphous carbon onto the surface of the active material following SCF treatment, likely facilitated adequate electron transport through an otherwise poorly conducting FeF_2 phase. Similarly, CoF_2 cells displayed high initial capacities (up to ~650 mA h g^{-1} at a potential of 1.2 V *vs.* Li/Li$^+$), although significant capacity fading ensued in the subsequent cycles. *Ex situ* XRD measurements confirmed a poor reversibility in the conversion sequence for CoF_2, with a complete loss of CoF_2 crystallinity and the sole presence of a crystalline LiF phase following charging.

1 Introduction

Since the advent of Li-ion battery technology, considerable research effort has focused on the discovery and development of electrode materials as candidates for future Li-ion batteries. In particular, nanostructuring of conventional cathode materials, namely $LiMO_2$ and $LiMPO_4$ (M = Fe, Co, Mn, Ni *etc.*), has attracted much focus, owing to shorter Li$^+$ diffusion lengths and hence, improved intercalation kinetics.[1,2] Whilst attractive, first–row transition metal oxides and phosphates suffer from relatively low Li$^+$ ion storage capacities (*e.g.*, ~170 mA h g^{-1} in the case of $LiFePO_4$), and thus their specific energies are limited. The requisite properties of future Li-ion batteries such as increased capacity, enhanced cyclability, rate performance, amongst others, coupled with their ever increasing popularity as drivers for modern and demanding electronic devices and electric/hybrid-electric vehicles (EV/HEVs) *etc.*, challenge researchers to seek ever more desirable materials with the properties to meet such rising demand.

In more recent times, researchers have considered the so-called 'conversion' electrodes as potential alternatives to the Li$^+$ intercalation host. The reason for their supposition lies with the inherent ability of the conversion candidate to utilise the full range of oxidation states available in the corresponding metal atom (Fe, Mn, Co *etc.*). The nature of such conversion chemistries typically results in redox transitions involving more than one electron and hence, the potential for greater specific capacities. Typical examples of conversion materials include transition metal oxides (MO_x), phosphides (MP_x), sulphides (MS_x), and fluorides (MF_x), and have been the subject of recent excellent review articles.[3,4] While conventional Li$^+$ intercalation hosts operate on the physical insertion and removal of Li$^+$ ions into and out of the local structure, conversion electrodes undergo their redox transitions in the absence of Li$^+$ intercalation, during which a complete reduction of the metal to form metallic nanoparticles of dimensions <5 nm, embedded in a matrix of Li–X (X = O, S, O, F *etc.*), results as depicted in eqn (1).[4]

$$M_aX_b + (bn)Li \leftrightarrow aM + bLi_nX \quad (1)$$

Initially, conversion materials were only considered useful as negative Li-ion electrodes owing to their relatively low operating potentials *vs.* Li/Li$^+$.[4] Metal fluorides, however, have been touted as one class of conversion materials with potential use as a positive electrode since the highly ionic nature of the M–F bond results in more feasible cathodic operating potentials. However, to their detriment, such high ionicity also renders potential MF_x candidates poorly conducting and, coupled with the formation of an insulating Li–X phase following their conversion, may lead

[a]Materials Chemistry & Analysis Group, Department of Chemistry and the Tyndall National Institute, University College Cork, Cork, Ireland

[b]Centre for Research on Adaptive Nanostructures and Nanodevices (CRANN), Trinity College Dublin, Dublin 2, Ireland

to a reduction in the efficiency of electron transfer and hence, poor electrochemical performance.

Iron(II) fluoride, FeF_2, which crystallises in a rutile, tetragonal structure (space group: P_42/mnm), is one such MF_x conversion candidate since it offers a high theoretical capacity ($\sim$571 mA h g^{-1}), at a theoretical electrode potential of 2.66 V *vs.* Li/Li^+.[5] Such attributes could potentially lead to FeF_2 cathodes displaying considerably higher energy densities compared to their intercalation analogues. The potentially high energy density may, however, be somewhat restrained as FeF_2 exhibits Mott-insulator properties.[6] Poor conductivity is an unfortunate and regular feature of many prospective Li-ion cathodes and is typically challenged by the addition of electrically conducting agents, *e.g.*, C, Cu, Ag *etc.*, to the electrode mix, or by grafting layers of such materials to the active material surface either *in situ* or *via* post-synthetic techniques. Further to such treatments, it is accepted that a move to nanoscale dimensions may influence properties such as electrical conductivity *versus* their bulk counterparts. As such, a tailored synthesis of MF_x conversion materials having improved electrode properties may permit their use in Li-ion technology.

Whilst several examples of iron(III) fluoride (FeF_3) cathodes have been reported in the literature, including nanowires,[7] thin-films,[8,9] carbon nanocomposites,[10–14] and the hydrated form, $FeF_3 \cdot 0.33H_2O$,[15] much less has been reported on the synthesis and electrochemical performance of the analogous FeF_2 phase alone. A recent report by Reddy *et al.* has shown C–FeF_2 to be a promising candidate.[16] It is important to note that, although the complete reduction of FeF_3 affords higher theoretical discharge capacities ($\sim$712 mA h g^{-1} *vs.* 571 mA h g^{-1}, respectively), at slightly higher electrode potentials (see Table 1), previous work has demonstrated an increasingly ineffective reconversion process in FeF_3 following successive charge–discharge cycling.[7] In addition, Yamakawa *et al.*[17] identified that charging of FeF_3 cells following electrochemical conversion was associated with a transition from an original ReO_3-type structure to that of a defective rutile phase. FeF_3 does, however, possess the inherent ability to insert $\sim$0.5 mol Li^+ before the onset of electrochemical conversion, which has led to its utilisation as a more typical intercalation electrode with capacities reported approaching 200 mA h g^{-1}, at voltages which are beyond the scope of FeF_2.[7,12,13,15] To this end, FeF_2 may be considered a somewhat more model conversion system, displaying reversible conversion character while beneficially involving fewer phase transitions compared to that of FeF_3. It should also be noted that the complete reduction products of FeF_2 and FeF_3 (Fe^0 and LiF), are theoretically equivalent, indicating a predictably similar electrochemical pathway should occur during their electrochemical conversion (subsequent to an initial $Fe^{3+} \rightarrow Fe^{2+}$ transition in FeF_3); the mechanism of which, is still a subject of heavy scrutiny.[18–21]

Cobalt(II) fluoride, CoF_2, which also crystallises in tetragonal form (space group P_42/mnm), is another interesting candidate not least given cobalt's extensive use in early generation Li-ion cells (as $LiCoO_2$). In addition, CoF_2 extends a theoretical capacity of $\sim$553 mA h g^{-1} at an electrode potential of 2.85 V *vs.* Li/Li^+, leading to theoretical energy densities as high as 1500 W h kg^{-1}. Previous studies,[22] however, have outlined an incompatibility of phase-pure thin-film CoF_2 electrodes in conventional organic-based electrolytes, which has led to their relatively low levels of evaluation as potential Li-ion conversion candidates. A partial stability of CoF_2 in organic electrolyte was achieved by depositing a layer of lithium phosphorus oxynitride (Lipon) onto the surface of CoF_2 thin-films by a pulsed laser deposition (PLD) process, where such coatings led to the limited cyclic evaluation of CoF_2 as a potential negative Li-ion electrode.[22] Phase-pure CoF_2 cathodes have also been evaluated by Wall *et al.*[23] which displayed high initial capacities ($\sim$600 mA h g^{-1} at 1.0 V *vs.* Li/Li^+), however, such cells also displayed significant capacity decline over 25 discharge–charge cycles. CoF_2 has therefore, been somewhat disregarded as a potential conversion electrode to-date, however, a review of its electrical properties with Li^+ is still a facet that should not be ignored.

Herein this paper details a novel supercritical fluid (SCF) synthesis of FeF_2 and CoF_2 powders using $[Fe(tta)_3]$ (tta = 4,4,4-trifluoro-1-(2-thienyl)-1,3-butanedionate), as a single-source precursor for the synthesis of FeF_2 powders and $[Co(hfac)_2 \cdot 2H_2O]$ (hfac = 1,1,1,5,5,5-hexafluoro-2,4-pentanedionate), similarly, for the synthesis of CoF_2 powders. Previously, $[Co(hfac)_2 \cdot 2H_2O]$ precursors have been used for the growth of CoO or Co_3O_4 thin films by metal–organic chemical vapour deposition (MOCVD),[24] while a similar Fe-based precursor, $[Fe(acac)_3]$ (acac = acetylacetonate), has been employed for the growth of Fe_2O_3 thin-films in supercritical CO_2.[25] This is the first apparent synthesis of Fe- and Co-containing fluorides using $[Fe(tta)_3]$ and $[Co(hfac)_2 \cdot 2H_2O]$ as single-source precursors by direct chemical routes. The as-obtained FeF_2 and CoF_2 electrodes display high initial discharge capacities (up to $\sim$1100 mA h g^{-1} at 1.0 V *vs.* Li/Li^+ in the case of FeF_2, and $\sim$600 mA h g^{-1} at 1.2 V *vs.* Li/Li^+ for CoF_2).

Table 1 The theoretical capacity and electrode potentials, *E* (*V*), of Fe- and Co-fluorides

Compound	Oxidation state	Theoretical capacity (mA h g^{-1})	*E* (*V*)
FeF_2	+2	571	2.66
FeF_3	+3	712	2.74
CoF_2	+2	553	2.85
CoF_3	+3	694	3.61

2 Experimental section

2.1 Supercritical fluid synthesis of FeF_2 powders

FeF_2 powders were synthesised using the β-diketonate, $[Fe(tta)_3]$ (iron (III)-thenoyltrifluoroacetonate), as a single-source precursor according to procedures reported in the literature.[26] 0.2 g of $[Fe(tta)_3]$ was dissolved in 15 ml of dry toluene and sonicated for 3–5 min to ensure complete dissolution. The $[Fe(tta)_3]$ precursor solution was then injected into a sealed SCF stainless steel reaction cell (24 ml total volume, High Pressure Equipment (HiP) company), and heated to 400 °C at a ramp rate of 30 °C min^{-1}, and held for 1 h. An illustrative representation of the batch SCF setup is displayed in Fig. 1. After 1 h, the SCF cell was cooled to room temperature naturally (high pressure

cells should never be quenched with liquids), and slowly depressurised. The FeF_2 product was isolated by decantation, washed with acetone to remove trace impurities and excess solvent and air-dried at room temperature for at least 24 h, forming the final brown-coloured powder product.

2.2 Supercritical fluid synthesis of CoF_2 powders

CoF_2 was prepared using $[Co(hfac)_2 \cdot 2H_2O]$ (cobalt (II)-hexafluoroacetylacetonate), as a single-source precursor which was used as received from Sigma-Aldrich and treated in a similar SCF batch method as described in 2.1. Typically, 0.2 g of $[Co(hfac)_2 \cdot 2H_2O]$ precursor was dissolved in toluene (15 ml) and sonicated for 3–5 min, before being injected into a sealed stainless steel reaction cell (24 ml total volume, HiP company), and heated to 400 °C at a heating rate of 30 °C min^{-1} and held at this temperature for 1 h. After 1 h, the reaction cell was cooled to room temperature and slowly depressurised. The CoF_2 product was isolated by means of decantation, washed with acetone to remove trace impurity and excess solvent and air-dried at room temperature for at least 24 h forming the final pink coloured powder.

2.3 Material characterisation

X-ray diffraction (XRD) measurements were performed on a Phillip's XPERT diffractometer using Cu Kα radiation (1.5406 nm) operating at 40 kV and 35 mA. Scanning electron microscopy (SEM) images were collected on a FEI Quanta 650 microscope operating at 10 kV and transmission electron microscopy (TEM) images were collected on a JEOL JEM 2100 TEM operating at 200 kV. Thermogravimetric analysis (TGA) was carried out at a heating rate of 40 °C min^{-1} in N_2 using a Mettler Toledo TGA/DSC1 STAR system.

For the electrochemical measurements, electrode slurries were prepared by mixing the active powder, acetylene black (Alfa Aesar, corp.), and PVDF (Sigma-Aldrich) in a ratio of 75 : 25 : 5 by mass, respectively. Absolute EtOH was used to ensure adequate consistency of the slurries. The slurries were then cast on to pre-cleaned Al-foil and dried at 120 °C for several hours before mechanically pressing and further drying at 120 °C for at least 24 h. CR2025-type coin cells were assembled in a glovebox filled with high purity Ar gas, using pure Li chips (MTI corp.), serving as the negative electrode and Celgard® 2320 PE/PP/PE membranes as separator. The electrolyte was a solution of 1 M $LiPF_6$ in EC : DMC (50 : 50 v/v). Galvanostatic cycling was carried out in the potential range between 1.0–5.0 V for FeF_2 and 1.2–4.8 V *vs.* Li/Li^+ for CoF_2, using a Princeton Applied Research (V3) potentio/galvanostat. Typical active loadings were in the order of 0.5–1 mg. Respective current densities and capacities were determined on the mass of active material loading.

3 Results and discussion

3.1 Synthesis and structural characterisation of FeF_2 powders

FeF_2 powders were prepared *via* a novel supercritical fluid synthesis using $[Fe(tta)_3]$ as a single-source precursor, dissolved in toluene. The reaction setup is depicted in Fig. 1. Supercritical conditions were attained by the batch-method by sealing the as-prepared precursor solution in a high pressure reaction cell, followed by the thermal treatment at 400 °C for 1 h. Previously, $[M(tta)_2]$ (M = Cd, Zn), single-source precursors have been used in the preparation of CdO, CdS or CdF_2 phases by a solution route,[27] and ZnO by a MOCVD route,[28] respectively, following coordination of the bis-complex precursor sphere with tmeda (*N*,*N*,*N*′,*N*′-tetramethylethylenediamine), to form the single-source precursor adduct $[M(tta)_2 \cdot tmeda]$. Similarly, the precursors $[Mg(hfac)_2]$ and $[Mg(TFacac)_2]$, (TFacac = 1,1,1-trifluoro-2,4-pentanedione), have been used to prepare MgF_2 films by the thermally-driven disproportionation and decomposition of the respective precursors at temperatures exceeding 500 °C.[29] The similarity of precursor composition in these instances outlines the role of synthetic conditions in directing the formation of either metal-oxide, sulphide or fluoride as the major product phase. Under supercritical CO_2 conditions, the non-fluorinated $[Fe(acac)_3]$ single-source precursor has been used in the preparation of Fe_3O_4,[25] however, this is the first apparent synthesis and direct formation of FeF_2 by means of either conventional thermal treatment or *via* a supercritical route using $[Fe(tta)_3]$ as a single-source precursor.

To elucidate potential FeF_2 formation under SCF conditions, a consideration of the thermal decomposition of $[Fe(tta)_3]$ is necessary, where the formation of either oxide, sulphide or fluoride as mixed or single phases may be expected depending on the nature of decomposition; the process of which, likely varies considerably as changes are employed to the reaction conditions (temperature, time *etc.*). Such phases are not easily distinguishable by means of TGA given that their expected residues are appreciably similar.[27] The variance in C–X (X = S, O, F), bond dissociation energies of $[Fe(tta)_3]$ (C=O = 799 kJ mol^{-1}, C–S = 272 kJ mol^{-1} and C–F = 490 kJ mol^{-1}), could possibly indicate a preference for the formation of a dominant FeS_x phase, however, XRD analysis (Fig. 2), of the brown powder product indicated the formation of tetragonal-phase FeF_2 as the single-phase reaction product (PDF: 81-2272), with reflections at 2θ values of 26.99, 33.31, 38.56, 43.17, 51.66, 55.40, 62.89, 66.10 and 69.68° corresponding to the (110), (101), (111), (210), (211), (220), (112), (301) and (202) set of planes in tetragonal FeF_2,

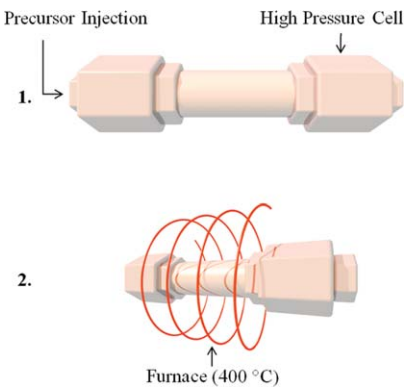

Fig. 1 Batch SCF reaction scheme used in the preparation of FeF_2/CoF_2 powders.

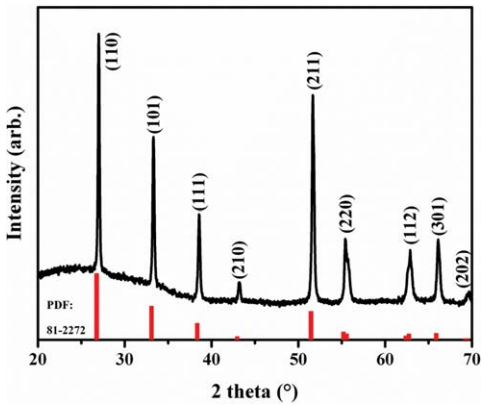

Fig. 2 XRD profile of FeF_2 powders obtained from the SCF synthesis of $[Fe(tta)_3]$ at 400 °C for 1 h. The red bar makers indicate the respective positions (2θ) of FeF_2 (PDF: 81-2272).

respectively. No impurity peaks belonging to sulphide or oxide phases, or otherwise originating from the analogous FeF_3 or other Fe^{3+} impurities, were discernible in the XRD profile. Interestingly, Malandrino *et al.*[27] have shown that an analogous $[Cd(tta)_2]\cdot$tmeda precursor adduct favoured the formation of CdO *via* a conventional solution route when thermal treatment was carried out between 300 and 700 °C under flowing O_2, while CdF_2 was favoured under flowing N_2 between 350 and 450 °C and CdS favoured above a temperature of 550 °C.[27] These results suggest that the formation of CdF_2 is favoured at the lower temperature region (350–450 °C), while dissociation of the C–F bond under such conditions is likely preferential to that of C–S, which is located within the heavily stabilised 5-membered ring of the respective thiophene group. Malandrino *et al.*[27] have also alluded to the possibility of CdS or S phase formation existing in non-crystalline form which could further react with CdF_2 to form CdS at the higher temperature regions.

In the case of FeF_2, a temperature of 400 °C was used to attain supercritical conditions (toluene) which likely facilitated a similar decomposition process of the $[Fe(tta)_3]$ precursor. TGA analysis of the $[Fe(tta)_3]$ precursor collected under flowing N_2 depicts a two-phase transition process resulting in the complete decomposition of the precursor over the temperature range between 400 and 450 °C. A two-phase transition commences with a ~1 wt% loss occurring at a temperature of ~165 °C (ascribed to the onset of precursor melting), followed by a decomposition step over the range 210–400 °C resulting in a further loss of ~93 wt% and a residue of ~6 wt%.

The formation of FeF_2 as a single phase component underlines SCF conditions were also favourable to the formation of Fe existing in the +2 oxidation state, given that no FeF_3 or other Fe^{3+} species were discernible in the XRD powder patterns; such an effect is particularly of note while the availability of F in the precursor was abundant and that the relative Gibbs energy of formation, ΔG_f, of FeF_3 is considerably lower than that of FeF_2 under standard conditions (−972 *vs.* −663 kJ mol^{-1}, respectively). It must also be suggested, however, that there lies a possibility of such Fe^{3+} phases existing in the amorphous state or critically, existing in feature size below the X-ray coherence length used in the evaluation of the product composition.

The morphology of the FeF_2 powders was investigated by SEM and is displayed in Fig. 3. The SEM images reveal the formation of a variety of different structures consisting of small-scale nanorods which widely assembled into urchin-like features, to larger, more-elongated ribbon-like structures. The diameter of these structures varied from approximately 100 nm (short nanorod structures) to the wider, up to ~2 μm sized elongated rods. TEM analysis of the FeF_2 structures (Fig. 3(d)), revealed a highly crystalline nature with an amorphous layer surrounding the FeF_2 domains, measuring approximately 5 nm in thickness. The clearly observable lattice fringes, which correspond to an inter-planar (d) spacing of 3.13 Å, may be indexed to the (110) set of planes in tetragonal FeF_2 (JCPDS: 81-2272), while the clearly defined lattice fringes visibly extend the length of the FeF_2 structure and confirm the high crystallinity of the FeF_2 powder. The ~5 nm amorphous layer may be attributed to the deposition of carbonaceous species following decomposition of the precursor or the organic reaction medium (toluene) used during preparation. The presence of amorphous carbon is also indicated in the XRD profile (shown in Fig. 2), displaying a broad (20–35° 2θ), bending region, a feature often characteristic of non-graphitic carbon types. The presence of carbon is further confirmed by Raman analysis, displayed in Fig. 4, which shows the D and G bands characteristic of sp^3 and sp^2 carbon types.

3.2 Synthesis and characterisation of CoF_2 powders

CoF_2 powders were synthesised under a similar SCF method following the thermal decomposition of the $[Co(hfac)_2\cdot 2H_2O]$ in supercritical toluene at 400 °C. The XRD profile of the as-obtained, pale-pink coloured CoF_2 powder is shown in Fig. 5.

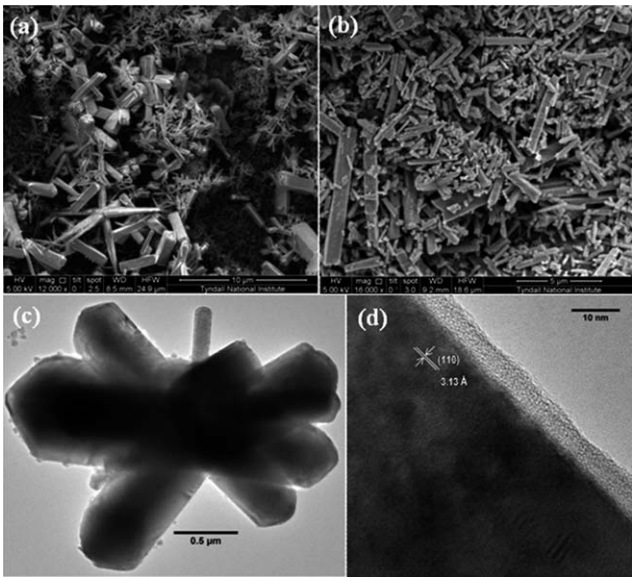

Fig. 3 (a and b) SEM images of FeF_2 obtained from $[Fe(tta)_3]$ at 400 °C in supercritical toluene (c and d) TEM images of FeF_2 obtained under the same conditions. The lattice spacing indicated in Fig. 3(d) may be indexed to the (110) set of planes in FeF_2 (JCPDS: 81-2272). Scale bar for 3(a) 10 microns, 3(b) 5 microns, 3(c) 0.5 microns and 3(d) 10 nm.

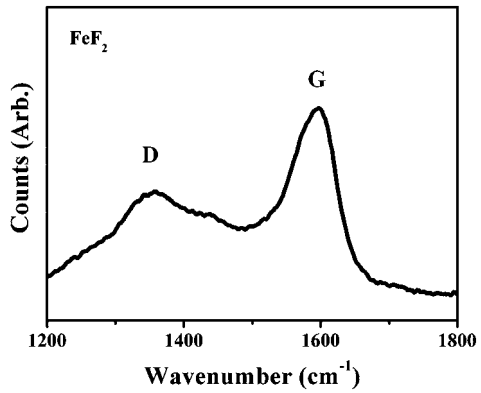

Fig. 4 Raman spectra of a FeF_2 powder sample collected over the range 1200–1800 cm^{-1}, showing D (sp^3) and G (sp^2) bands characteristic of carbon types.

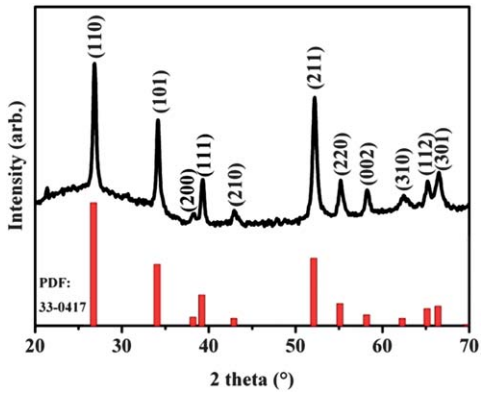

Fig. 5 XRD profile of CoF_2 powders obtained from the SCF synthesis of [$Co(hfac)_2 \cdot 2H_2O$] at 400 °C for 1 h. The red bar makers indicate the respective positions (2θ) of CoF_2 from PDF pattern no. 33-0417.

The crystal reflections at 2θ values of 26.83, 34.14, 38.20, 39.26, 42.90, 52.19, 55.17, 58.21, 62.22, 65.26 and 66.50° correspond to (110), (101), (200), (111), (210), (211), (220), (002), (310), (112) and (301) set of planes in tetragonal CoF_2 (PDF: 33-0417), respectively, and confirms the presence of CoF_2 existing as the major product phase. A similar bending region in the XRD profile (20–35° 2θ) was also observed, and is ascribed to the existence of amorphous carbon. The thermal decomposition of [$Co(hfac)_2 \cdot 2H_2O$] is predictably less complex than that of [$Fe(tta)_3$] given the likely possibility of forming just two separate phases as the major product (Co_xO_y and CoF_x), as opposed to a third MS_x phase. In this instance, the formation of CoF_2 was pronounced under supercritical conditions at 400 °C with such conditions favouring the formation of Co in the +2 oxidation state while the availability of F in the [$Co(hfac)_2 \cdot 2H_2O$] precursor (12 F^- per formula unit), was markedly abundant. The possibility of forming Co_xO_y phases was also considered, however, the apparent lack of oxide formation as a result of supercritical processing (in what is a closed reaction system), may be explained by the lack of available oxygen existing in the reaction medium (toluene), coupled with the strong dissociation energy of the C=O bond of the precursor (C=O = 799 kJ mol^{-1}). Such an effect would also describe the lack of Fe_xO_{x+1} phases resulting from the supercritical processing of [$Fe(tta)_3$] under similar conditions. A direct comparison of the relative Gibbs' energy of formation for the respective phases (Co_xO_y, CoF_2), is difficult in this instance, given the large deviation from standard conditions under SCF processing.

SEM analysis of the CoF_2 powder samples indicated the formation of near-uniform spherical morphologies, ranging in diameter from 0.7–1.8 μm as shown in Fig. 6(a) and (b). Closer inspection of the CoF_2 spheres revealed a distinctive surface roughness, indicating that the spheres are comprised of a series of smaller, nanoscale features of an acicular-like crystal type. Higher resolution TEM images displayed in Fig. 6(c) and (d), confirmed that the larger CoF_2 spheres formed from a series of dendritic-like structures, whose feature sizes ranged between 20 and 30 nm in diameter. The nanoscale featuring of the CoF_2 powders in this instance may enhance the size of the electrode–electrolyte interface *versus* the respective bulk counterpart; such properties may possibly favour Li^+ transport by facilitating improved electrolyte access. It must also be considered, however, that such increases in the available surface area compared to that of the bulk phase may augment the formation of unwanted side interactions with the electrolyte, resulting in increases in respective decomposition products.

3.3 Li^+ induced conversion of FeF_2 powders

Table 1 summarises the theoretical electrode potentials and capacities of Fe- and Co-fluorides, outlining their practical use as potential positive electrodes in Li-ion technology; theoretical electrode potentials, E (V), are given in the literature.[5] Our study has focused on the synthesis of FeF_2 and CoF_2 powders and their use as prospective Li-ion cathodes since the equilibrium

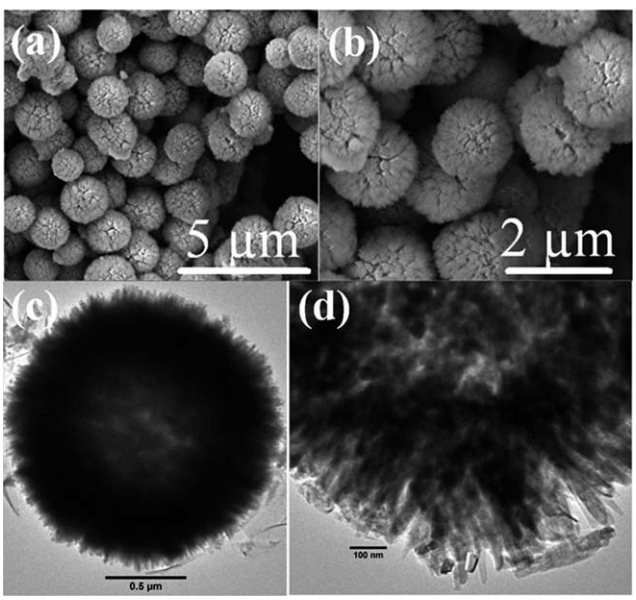

Fig. 6 (a and b) SEM images of CoF_2 spheres obtained at 400 °C from [$Co(hfac)_2 \cdot 2H_2O$] using supercritical toluene and (c and d) TEM images of CoF_2 spheres obtained under the same conditions.

potentials of FeF_2 and CoF_2 fall within feasible limits for such applications. Although the corresponding tri-fluoride phases afford higher theoretical energy densities given their increased working potentials and capacities (Table 1), much less has been reported on the model MF_2 conversion systems alone.

The equilibrium potential of FeF_2 is predicated from thermodynamic considerations at 2.66 V *vs.* Li/Li^+ (Table 1). Such potentials are considerably higher than those afforded by the ferric oxides, sulfides and phosphides, outlining the practical use of FeF_2 as a positive Li-ion electrode.[30,4] The premise of the FeF_2 conversion mechanism assumes the reversible reaction as depicted in eqn (2). Although the complete mechanism is somewhat bypassed in this form, the formation of LiF and Fe^0 accounts for the complete reduction of Fe^{2+} in the original species *via* a $2e^-$ process, resulting in a theoretical capacity of ~571 mA h g^{-1}. Such capacities are considerably higher than those afforded by conventional intercalation hosts such as $LiFePO_4$ (~170 mA h g^{-1}), and $LiCoO_2$ (~120 mA h g^{-1}) and lead to vast specific energies exceeding 1500 W h kg^{-1}.

$$FeF_2 + 2Li^+ + 2e^- \rightarrow Fe^0 + 2LiF \quad (2)$$

The first discharge curves of the FeF_2 cells cycled at a lower cut-off potential of 1.0 *vs.* Li/Li^+ at the current densities of 10 and 20 mA g^{-1} (~0.017 and 0.035 C rate, respectively), are displayed in Fig. 7(a). Both discharge profiles show a sloping voltage region commencing at ~2.6 V *vs.* Li/Li^+ (open circuit voltage = 2.95 V), which accounts for some ~50 mA h g^{-1} of the total capacity obtained in the first cycle. A portion of this sloping region may be attributed to the formation of solid electrolyte interphase (SEI) layers on the active material surface: initially, such passivation layers were only considered for lithium or carbon anodes, however, research has confirmed the existence of the SEI layer on cathodic surfaces, including that of FeF_x.[17] Such occurrences may arise as a result of spontaneous contact with electrolyte or predictably, during normal electrochemical operation, however, no structural confirmation of this layer is presented. Additionally, a number of other possible mechanisms have been predicted which could account for the initial sloping region, preceding the onset of electrochemical conversion. Although the existence of impurity Fe^{3+} phases, including that of FeF_3, were not detected in the XRD profile (Fig. 2), a reduction of trace amounts of amorphous Fe^{3+} phases must be considered; indeed, the reduction of Fe^{3+} phases is known to occur in the 3.0–2.0 V region and is thus a distinct possibility.[17] Conversely, a number of conversion-competing processes have also been proposed,[17,18] although there remains some degree of uncertainty as to their proposition. Yamakawa *et al.*[17] studied the local structures formed as a result of cycling FeF_x cathodes by Li^6 and F^{17} solid-state NMR coupled with *ex situ* XRD measurements, and concluded that the early stages of discharge in FeF_2 involved both intercalation and conversion processes. It is generally accepted that reduction of Fe^{2+} to Fe^{1+} is unlikely *via* simple 1 × 1 tunnelling, thus any possible intercalation is likely to proceed following reduction of Fe^{3+} impurity, or *via* the formation of intermediate species formed as a result of a disproportionation reaction of FeF_2 to form Fe^0 and Fe^{3+} species, outlined in eqn (3)–(6).[17]

$$FeF_2 \rightarrow Fe_{1-x}F_2 + Fe \quad (3)$$

$$Fe_{1-x}F_2 + {}_x\!Li \rightarrow Li_xFe_{1-x}F_2 \quad (4)$$

$$Fe_{1-3x}{}^{2+}Fe_{2x}{}^{3+}F_2 \rightarrow Li_{2x}Fe_{1-x}F_2 \quad (5)$$

$$Li_{2x}Fe_{1-x}F_2 \rightarrow {}_{2y}\!LiF + Li_{2x-2y}Fe_{1-x}F_{2-2y} \quad (6)$$

The first step (eqn (3)) proposed by Yamakawa *et al.*,[17] involves the lithium-driven displacement of Fe from the FeF_2 lattice, forming Fe^0 and Fe^{3+}, whilst also maintaining a rutile $Fe_{1-x}F_2$ structure. Such structures are thought to accommodate the insertion of Li^+ ions in a more typical intercalative fashion. The possibility of further Li^+ insertion to form $Li_x[Li_xFe_{1-x}]F_2$ is also considered. The reactions such as those proposed in eqn (3) to (6), are believed to fall within the 3.0–2.0 V voltage window and could potentially compete with an onset of the conversion reaction outlined earlier in eqn (2). In support of this fact, molecular dynamic simulations have also predicted early intercalation in FeF_2 cathodes by means of analysing Li^+ exposure to the low energy (001) and (110) surfaces of FeF_2, where it was identified that a competitive process existing between Li^+ intercalation along [001] channels and that of electrochemical conversion results.[18] Such mechanisms are suggested to be widely governed by the rate of discharge and crystal orientation of the FeF_2 local structure during exposure to Li^+.[18] Such a competitive mechanism is, however, challenged somewhat by experimental observation that FeF_2 undergoes a rapid structural conversion mechanism in the absence of intercalation to the corresponding Fe^0 and LiF phases with no Fe^+ intermediaries.[19,20] A recent communication by Wang *et al.*[21] has also depicted the conversion process of FeF_2 for the first time by *in situ* TEM observation. The authors found a surprisingly fast conversion process occurs (several minutes for FeF_2

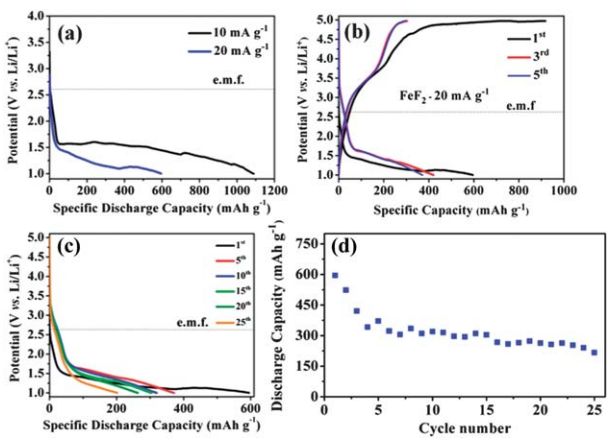

Fig. 7 (a) 1st discharge curves of FeF_2 powders to 1.0 V *vs.* Li/Li^+ at the current densities of 10 (black line) and 20 (blue line) mA g^{-1}, (b) 1st, 3rd and 5th discharge–charge curves obtained at a constant current of 20 mA g^{-1}, (c) 25-cycle discharge curves at the same current rate and (d) discharge capacity as a function of cycle number.

nanoparticles), forming small diameter (1–3 nm) metallic Fe^0 nanoparticles, surrounded by an amorphous LiF phase which ensued as a result of a propagation of a reaction front through the active FeF_2 domains. The absence of any identifiable Fe^{3+} phases by electron energy loss spectroscopy (EELS) measurements suggested that the conversion mechanism followed an intermediary pathway although, notably, the authors also suggest the possibility of Li^+ intercalation resulting in supersaturation of the FeF_2 host resulting in a transformation from a crystalline rutile structure to that of an amorphous phase which could be responsible for the lack of detection of a lithiated (intercalated), phase by means of electron diffraction measurements.[21] Following on from the early sloping region in our discharge profile (Fig. 7), a long plateauing region develops which is attributed to the relevant phase transition(s) associated with the electrochemical conversion reaction of FeF_2. At the lower current density of 10 mA g^{-1} ($\sim$0.035 C rate, 1 C = 571 mA g^{-1}), the onset of plateauing ensues from $\sim$1.65 V before showing very gradual decline over the remainder of the discharge process. After reaching a potential limit of 1.0 V, the capacity obtained following the first discharge cycle was $\sim$1100 mA h g^{-1}, representing approximately twice that of the theoretical capacity assumed for a $2e^-$ conversion process in FeF_2. On increasing the current rate to 20 mA g^{-1}, the discharge profile displayed a gradual decline over the first $\sim$400 mA h g^{-1}, followed by an inflection from $\sim$1.5 V before a slight plateau region ensued nearer the low-voltage limit. After reaching a potential limit of 1.0 V, the capacity returned was some 590 mA h g^{-1}, representing only a slight over-capacity with respect to theoretical maxima (571 mA h g^{-1}); in both cases, the high capacities returned outlines the highly promising potential of FeF_2 during early stages of electrochemical cycling. The disparity in capacity and the nature of discharge between the comparative current densities does, however, indicate a large degree of sensitivity of the conversion process to the applied discharge rate. Such a result is not surprising given the current understanding of the relatively sluggish kinetics of the conversion sequence, coupled by a predictably high incidence of overpotential which arises from poor electronic conductivity and polarisation effects.

The first, third and fifth discharge–charge (voltage) curves for the FeF_2 cells taken at a current density of 20 mA g^{-1} over the same potential range are displayed in Fig. 7(b), while the 25-cycle discharge curves are shown in Fig. 7(c), depicting the evolution of the discharge process. The average discharge potential displayed increases slightly with respect to the initial conversion reaction (black line, Fig. 7(b)), which is likely due to the dramatically reduced active material size, resulting as a consequence of electrochemical conversion, thus leading to enhanced efficiency in the subsequent electrochemical conversion cycles. Notably, the first charge curve to 5.0 V (black line), displays a somewhat significant overcharge region, the nature of which may be ascribed to increases in SEI formation at elevated potential. Such overcharge, however, remains relatively insignificant following the first cycle which would also corroborate its attribution to instances of SEI formation during the first charge cycle. While potentially detrimental, the high charge voltage was necessary in order to attain appreciable cycling for our FeF_2 powders (see later). Also apparent, is the distinct observation of disparity between the relevant shapes of the discharge and charge curves, a feature of hysteresis which is both a common and undesirable feature of the conversion electrodes.[4]

Previously, it was shown that charging of FeF_3 cells at potentials up to 4.0 V results in the recovery of a lithiated-$Li_{0.5}FeF_3$ phase while further charging of FeF_3 cells to 4.5 V results in an initial recovery of a defect tri-rutile FeF_3 phase.[7] To this end, capacity fading has been expressed as a consequence of a poor reversibility in conversion sequence and has been observed by *ex situ* TEM/electron diffraction measurements, which depicts the co-existence of α-Fe and LiF phases existing with FeF_3 after successive (50) charge cycles.[7] Such incidences may suggest higher charging potentials may be required over time. In our case, charging the FeF_2 cells below 4.5 V, even at the relatively low current density of 20 mA g^{-1}, resulted in poor Coloumbic efficiency ($Q_{charge}/Q_{discharge}$), leading to poor capacity retention over relatively few discharge–charge cycles (not shown).

Fig. 7(d) displays the cycling performance of our FeF_2 powders at a current density of 20 mA g^{-1}. The specific capacity of the first discharge at a potential limit of 1.0 V was $\sim$590 mA h g^{-1}, representing a conversion of approximately 2.1 Li^+ per formula unit FeF_2. In the second cycle, a reduction in capacity is observed after formation of the SEI layer, however, the discharge capacity at this stage is still largely agreeable with the theoretical approximations based on a total reduction of Fe^{2+} in FeF_2 ($\sim$571 mA h g^{-1}). The midpoint voltage displayed over the discharge curve was $\sim$1.38 V, therefore representing a second-cycle energy density of 715 W h kg^{-1}; energy densities of this magnitude are considerably higher than those which may be afforded by conventional Li-ion intercalation cathodes such as $LiFePO_4$ ($\sim$610 W h kg^{-1}). A degree of capacity fading was evident over the first four cycles, however, some stabilisation of capacity was attained notably over the first 15 cycles at $\sim$300 mA h g^{-1}, while a discharge capacity of $\sim$220 mA h g^{-1} was returned following 25 charge–discharge cycles, representing a final conversion of approximately 1.1 Li^+ per formula unit FeF_2. Such capacities are largely similar to C–FeF_2 nanocomposites discharged to 1.3 V after the same number of cycles,[16] and still superior to theoretical capacities exhibited by some of the more conventional intercalation hosts, *e.g.*, $LiCoO_2$ ($\sim$120 mA h g^{-1}) and $LiFePO_4$ ($\sim$170 mA h g^{-1}); the lower average working voltage and low current rate of FeF_2 remains, however, potentially significant.

Although the discharge capacity of FeF_2 remained appreciable over the cycling period, the large degree of overpotential leads to large round-trip energy inefficiencies which may currently preclude their use in commercial environments. In addition, the high charging potentials required may lead to dramatic increases in electrolyte oxidation products, *e.g.*, FeF_6, LiF_6, $LiP_xO_yF_z$, resulting in abject increases in SEI formation which could potentially lead to increased levels of capacity fading. In addition, the rate capability of FeF_x-based electrodes, owing to their intrinsically poor conductivity and the relatively

limited kinetics of the conversion sequence, is also an issue facing the utilisation of FeF_x and other similar conversion candidates. The data reported in this work so far was collected at the relatively low specific currents of 10 and 20 mA g^{-1}, while cycling at an elevated current density of 200 mA g^{-1} (~0.35 C rate), resulted in a discharge capacity of just ~72 mA h g^{-1} after 25 cycles (not shown). FeF_2, therefore, may find limited application in future high-rate Li-ion batteries due to its sluggish and complex conversion chemistries. Such examples depend on rapid Li^+ diffusion kinetics which are ill-afforded in this case, and may depend on suitable open host structuring. Although the conversion kinetics of FeF_2 are demonstrated to be cumbersome at room temperature, both Reddy[16] and Badway *et al.*[10] have shown a vast improvement of equivalent carbon-composite FeF_2 cathodes operating at 40 and 70 °C, respectively. Interestingly, the operation of FeF_2 cathodes at 70 °C was largely similar to those of C/FeF_3 cells cycled at 25 °C, indicating the rate limiting steps during conversion of FeF_x lie at potentials <2.0 V.

3.4 Li^+ induced conversion of CoF_2 powders

Theoretically, CoF_2 extends the possibility of delivering a high capacity of 553 mA h g^{-1} at a slightly increased electrode potential compared to FeF_2 (2.85 V *vs.* Li/Li^+; see Table 1), resulting in potentially high energy densities exceeding 1500 W h kg^{-1}. The acicular-like CoF_2 powders prepared by our SCF route (displayed in the SEM images, Fig. 6), are a potentially useful morphology in electrode technology, and beyond, owing to an increase in the tapped density provided by their spherical structuring, while in addition, the nanoscale structuring which comprises the overall CoF_2 form, allows for an increased size of the electrode–electrolyte interface, and offering shorter Li^+ diffusion paths. While such characteristics have important implications for conventional intercalation hosts, such as favourable Li^+ transport, much less is known about such influences on conversion-type electrodes which undergo significant morphological changes as a result of their conversion. To this end, the influence of starting morphology on the first and subsequent discharge cycles remains unclear; however, it is reasonable to stipulate that an overall reduction in the size of the active material prior to conversion may facilitate an enhancement in the respective conversion kinetics. While these features are implicated before the initial discharge state, much less consideration is given to these effects after successive electrochemical cycling in which the active metallic species are already cycled between significantly smaller nano-sized features. Recently, Li *et al.*[7] reported the ability of FeF_3 nanowire architectures to largely maintain their overall structuring on cycling by forming a network of interconnected α-Fe domains, surrounded by a matrix of LiF. Equivalent data has not been presented for CoF_2 architectures, although a similar pathway is predicted.

The overall electrochemical conversion reaction of CoF_2 is outlined in eqn (7), where the expected sequence affords LiF and Co^0 as the reduction species in a $2e^-$ process. Previous reports of CoF_2 architectures operating as conversion candidates have thus far been limited due to an instability of CoF_2 in conventional liquid organic electrolytes. Fu *et al.*[22] prepared LiPON-coated CoF_2 thin-films by a PLD method, which delivered a capacity in the first discharge of ~600 mA h g^{-1} at the anodic potential limit of 0.01 V *vs.* Li/Li^+, while the introduction of their pure CoF_2 thin-films to the electrolyte solution resulted in severe instability. In this case, the introduction of LiPON coatings to the CoF_2 thin-film surface was thought to facilitate a reduction in the unfavourable interaction with liquid electrolyte, serving as a physical barrier layer in preventing its dissolution. The reduction species were confirmed by *ex situ* XRD measurements, signified by LiF (220) and Co (111) reflections in the XRD profile.[22] Recently, Wall *et al.*[23] prepared both CoF_2/C and Co/LiF/C composite cathodes without such protective features; although the CoF_2/C composite displayed higher initial capacity than that of the Co/LiF/C composite (~600 and ~150 mA h g^{-1} in the first discharge cycle, respectively), the Co/LiF/C composites displayed good capacity retention while the CoF_2/C composites attained just 15% capacity retention within the cycling period (50 cycles). The application of Co/LiF in composite form has also been displayed with meritable results.[31] In the case of our SCF-prepared CoF_2 powders, little visible interaction with the electrolyte solution ($LiPF_6$ dissolved in EC : DMC 50 : 50 vol%) was evident. The apparent stability of the CoF_2 powders in electrolyte was ascribed to the potential formation of carbon surfaces following the decomposition of both precursor and residual toluene during synthetic processing. To this end, evaluation by galvanostatic cycling was possible (Fig. 8), although consideration must be given to the long term influence of stability of CoF_2 with progressive electrochemical cycling in liquid organic electrolytes.

Limited data is available thus far with regards to detailed conversion mechanisms in CoF_2, although it has been proposed that CoF_2 extends an incomplete conversion mechanism with a further possibility of reaction between the newly formed

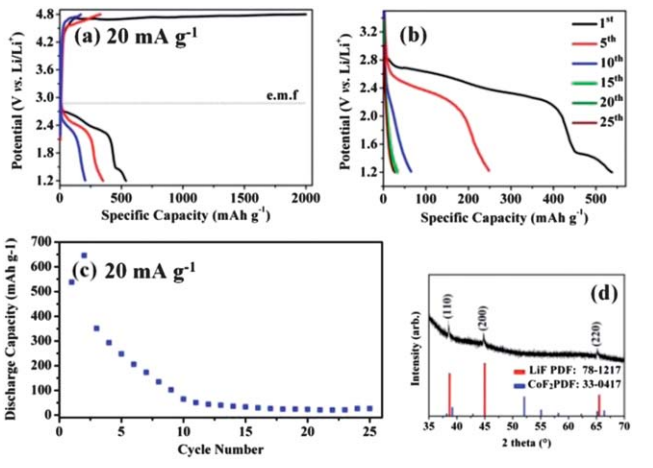

Fig. 8 CoF_2: (a) 1st, 3rd and 5th voltage curves at a current density of 20 mA g^{-1} (b) 25 cycle discharge curves at the same rate (c) discharge capacity as a function of cycle number and (d) *ex situ* XRD pattern of CoF_2 cells collected at the 25th charge-cycle.

nanograins of metallic Co^0 with LiF (eqn (7)), the process of which is outlined in eqn (8) & (9).[22]

$$CoF_2 + 2Li + 2e^- \leftrightarrow Co + 2LiF \quad (7)$$

$$xCo + LiF \leftrightarrow (1 - x)LiF + xFCo + xLi^+ \quad (8)$$

$$(1 - x)LiF + xFCo + xLi^+ + xe^- \leftrightarrow xCo + LiF \quad (9)$$

Fig. 8(a) shows the initial discharge–charge curves of the CoF_2 powders prepared by SCF synthesis. At a discharge potential limit of 1.2 V in the first cycle, a capacity of ~535 mA h g^{-1} was obtained, representing ~97% of the theoretical discharge capacity with respect to a full $2e^-$ conversion reaction of CoF_2 (~553 mA h g^{-1}). Thus far, first discharge capacities of this magnitude for CoF_2 conversion systems have only recently been reported.[23] A similar capacity (~600 mA h g^{-1}), was also obtained at the anodic potential limit of 0.01 V,[22] although the use of such voltages preclude their direct comparison. The first discharge profile extends a dual plateauing system with such regions extending from ~2.7 and 1.5 V *vs.* Li/Li^+. The first plateauing region (~2.7–2.3 V), accounts for some ~400 mA h g^{-1} of the total discharge capacity obtained, while the lower plateauing region (~1.5–1.2 V), is significantly shorter, accounting for ~130 mA h g^{-1}. Oxidation (fluorination) steps are discernable in the voltage curves, appearing as a sloping region from 4.3–4.6 V followed by a long, flat charge profile occurring from 4.6–4.8 V. The total charge capacity obtained at the upper cut-off potential was ~2000 mA h g^{-1}, representing significant overcharge compared to that of the first discharge capacity (535 mA h g^{-1}). Such an event indicates that complete charging of the CoF_2 cells overlaps the potential regions where the formation of electrolyte oxidation products is known to occur, through which may culminate in concomitant increases in unwanted electrolytic side reactions. Interestingly, the discharge capacity increased in the second cycle to ~650 mA h g^{-1}, which is significantly higher than predicted; the possibility of an insertion/interaction of metallic Co with LiF to form a CoLiF intermediary has been proposed,[22] although there is no evidence for this in our study. The third and subsequent discharge cycles offered declining capacity performance, however, the dual-plateauing regions which extend throughout the discharge profile offer somewhat similarity to those of the first cycle and suggests a similar yet increasingly inefficient sequence of electrochemical reductions occurred. Fu *et al.*[22] have shown that the first discharge reaction (eqn (7)) is largely irreversible, while the charge reaction of Co^0 and LiF affords CoF_x (here, $x < 1$), with only ~50% of the Co^0 and LiF re-converted to CoF_2 in the re-conversion process. The poor reversibility in the conversion sequence would account for the >70% loss of capacity experienced following the first few cycles, which results in a return of ~100 mA h g^{-1} after 10 cycles, while further cycling afforded yet further capacity decline, resulting in just ~30 mA h g^{-1} following the cycling period (25 cycles). In support of a poorly reversible sequence, the final phases in the charged CoF_2 cells were identified by *ex situ* XRD measurements (Fig. 8 (d)). The collected XRD patterns indicated a loss of CoF_2 crystallinity following cycling, with no discernible peaks originating from the starting CoF_2 phase. Broad peaks identifiable at 2θ values of 38.5, 44.8 and 65.3° may however, be indexed to the crystal reflections of the (110), (200) and (220) set of planes in LiF (PDF: 78-1217). The apparent loss of CoF_2 crystallinity as detected by XRD measurements would indicate that all of the original CoF_2 phase participated in the earlier conversion (discharge) reaction, while the charging process was either incomplete, or that the resultant CoF_x phase that reformed was amorphous or sufficiently small so as to exceed the X-ray coherence length. Further, no reflections originating from Co phases could be identified to indicate the reversibility of the system. The indication of crystalline LiF existing in the charged state, however, supports the notion of a poorly reversible conversion mechanism as proposed by Fu *et al.*[22] An *in situ* analysis of CoF_2 conversion with Li^+ is therefore preferential in order to best understand the mechanistic and structural evolution in the conversion sequence. While the specific capacity and operating voltage of CoF_2 remains agreeable with magnitudes that theoretical considerations would predict, improved electrochemical performance of CoF_2, particularly pertaining to extended cycle life, may result from a complete understanding of the conversion sequence. The optimisation of CoF_2 electrodes, such as the grafting of electrically conducting layers to the CoF_2 surface, could result in enhanced conversion kinetics and a more favourable re-conversion process, while the development and utilisation of alternative electrolyte compositions more suited to the operating potentials could allow further study of the respective cycling processes. A thorough understanding of the conversion mechanisms and the respective kinetics involved may allow for complete utilisation of CoF_2 with stable performance as a future Li-ion electrode.

4 Conclusions

In conclusion, a method of synthesising FeF_2 powders using a novel SCF route using $[Fe(tta)_3]$ as a single-source precursor in toluene at 400 °C was presented. CoF_2 powders were also prepared under a similar approach, using $[Co(hfac)_2 \cdot 2H_2O]$ serving as single-source precursor. This represents the first display of utilising such precursors in the formation of highly crystalline MF_2 powders under supercritical conditions. TEM analysis revealed an amorphous layer (~5 nm), surrounding the FeF_2 domains, which was ascribed to the deposition of carbonaceous species following the synthetic treatment under SCF conditions. Due to the intrinsically insulating nature of FeF_2, the conducting carbon layers surrounding the FeF_2 domains likely enabled adequate electron transfer. The FeF_2 cells display high initial energy capacities (up to 1100 mA h g^{-1} and 595 mA h g^{-1} at 10 and 20 mA g^{-1}, respectively), and are relatively stable over 25 discharge–charge cycles. A second discharge energy density of 810 W h kg^{-1}, which is significantly higher than those afforded by the conventional intercalation electrodes such as $LiFePO_4$ and $LiCoO_2$, outlines the high-potential of FeF_2 cathodes. The kinetics of the FeF_2 conversion sequence were appreciably poor at room temperature, however, resulting in diminished electrochemical performance at increased discharge rates. In addition, the relatively low average working

potential of FeF_2 (a deviation of >1.0 V per the calculated e.m.f), coupled with a large overpotential remains pertinent. Further work is required in order to assess the potential of FeF_2 cathodes with improved rate performance, which may be achieved by further reducing the active particle size or through the introduction of dopant species.

CoF_2 spheres, which were comprised of nanorods in the order of 20 nm diameter, also displayed appreciable capacity during early stages of electrochemical cycling, however, an unfavorable re-conversion mechanism and a possible ill-reaction with the organic electrolyte rendered the SCF prepared phase-pure CoF_2 a poor Li-ion electrode after relatively few electrochemical cycles. However, through the advancement of electrolyte compositions which are stable at higher voltages, or *via* composite formation, CoF_2 cannot be disregarded as a potential positive electrode at this stage.

Acknowledgements

This work was supported by Science Foundation Ireland (SFI) (Grants: 07/SRC/I1172, 08/CE/I1432 and 09/SIRG/I1621). This research was also enabled by the Higher Education Authority Program for Research in Third Level Institutions (2007-2011) via the INSPIRE program. The authors acknowledge the facilities and technical assistance from the staff at Electron Microscopy and Analysis Facility (EMAF) at Tyndall National Institute.

References

1 P. Poizot, S. Laruelle, S. Grugeon, L. Dupont and J. M. Tarascon, *Nature*, 2000, **407**, 496–499.
2 J. M. Tarascon and M. Armand, *Nature*, 2001, **414**, 359–367.
3 R. Malini, U. Uma, T. Sheela, M. Ganesan and N. G. Renganathan, *Ionics*, 2009, **15**, 301–307.
4 J. Cabana, L. Monconduit, D. Larcher and M. R. Palacín, *Adv. Mater.*, 2010, **22**, E170–E192.
5 G. G. Amatucci and N. Pereira, *J. Fluorine Chem.*, 2007, **128**, 243–262.
6 G. Valerio, M. Catti, R. Dovesi and R. Orlando, *Phys. Rev. B: Condens. Matter*, 1995, **52**, 2422–2427.
7 L. Li, F. Meng and S. Jin, *Nano Lett.*, 2012, **12**, 6030–6037.
8 Y. Makimura, A. Rougier, L. Laffont, M. Womes, J.-C. Jumas, J.-B. Leriche and J.-M. Tarascon, *Electrochem. Commun.*, 2006, **8**, 1769–1774.
9 Y. Makimura, A. Rougier and J.-M. Tarascon, *Appl. Surf. Sci.*, 2006, **252**, 4587–4592.
10 F. Badway, F. Cosandey, N. Pereira and G. G. Amatucci, *J. Electrochem. Soc.*, 2003, **150**, A1318–A1327.
11 I. Plitz, F. Badway, J. Al-Sharab, A. DuPasquier, F. Cosandey and G. G. Amatucci, *J. Electrochem. Soc.*, 2005, **152**, A307–A315.
12 N. Yabuuchi, M. Sugano, Y. Yamakawa, I. Nakai, K. Sakamoto, H. Muramatsu and S. Komaba, *J. Mater. Chem.*, 2011, **21**, 10035–10041.
13 S.-W. Kim, D.-H. Seo, H. Gwon, J. Kim and K. Kang, *Adv. Mater.*, 2010, **22**, 5260–5264.
14 S.-T. Myung, S. Sakurada, H. Yashiro and Y.-K. Sun, *J. Power Sources*, 2013, **223**, 1–8.
15 C. Li, L. Gu, S. Tsukimoto, P. A. van Aken and J. Maier, *Adv. Mater.*, 2010, **22**, 3650–3654.
16 M. A. Reddy, B. Breitung, V. S. K. Chakravadhanula, C. Wall, M. Engel, C. Kübel, A. K. Powell, H. Hahn and M. Fichtner, *Adv. Energy Mater.*, 2013, **3**, 308–313.
17 N. Yamakawa, M. Jiang, B. Key and C. P. Grey, *J. Am. Chem. Soc.*, 2009, **131**, 10525–10536.
18 Y. Ma and S. H. Garofalini, *J. Am. Chem. Soc.*, 2012, **134**, 8205–8211.
19 S. Rangan, R. Thorpe, R. A. Bartynski, M. Sina, F. Cosandey, O. Celik and D. D. T. Mastrogiovanni, *J. Phys. Chem. C*, 2012, **116**, 10498–10503.
20 F. Wang, R. Robert, N. a. Chernova, N. Pereira, F. Omenya, F. Badway, X. Hua, M. Ruotolo, R. Zhang, L. Wu, V. Volkov, D. Su, B. Key, M. S. Whittingham, C. P. Grey, G. G. Amatucci, Y. Zhu and J. Graetz, *J. Am. Chem. Soc.*, 2011, **133**, 18828–18836.
21 F. Wang, H.-C. Yu, M.-H. Chen, L. Wu, N. Pereira, K. Thornton, A. Van der Ven, Y. Zhu, G. G. Amatucci and J. Graetz, *Nat. Commun.*, 2012, **3**, 1201.
22 Z.-W. Fu, C.-L. Li, W.-Y. Liu, J. Ma, Y. Wang and Q.-Z. Qin, *J. Electrochem. Soc.*, 2005, **152**, E50–E55.
23 C. Wall, R. Prakash, C. Kübel, H. Hahn and M. Fichtner, *J. Alloys Compd.*, 2012, **530**, 121–126.
24 A. Gulino, G. Fiorito and I. Fragalà, *J. Mater. Chem.*, 2003, **13**, 861–865.
25 S. De Dea, D. Graziani, D. R. Miller and R. E. Continetti, *J. Supercrit. Fluids*, 2007, **42**, 410–418.
26 (*a*) E. W. Berg and J. T. Truemper, *J. Phys. Chem.*, 1960, **64**, 487–490; (*b*) H. Soling, *Acta Chem. Scand., Ser. A*, 1976, **30**, 163–170.
27 G. Malandrino, S. T. Finocchiaro, P. Rossi, P. Dapporto and I. L. Fragalà, *Chem. Commun.*, 2005, **8**, 5681–5683.
28 G. Malandrino, M. Blandino, L. M. S. Perdicaro, I. L. Fragalà, P. Rossi and P. Dapporto, *Inorg. Chem.*, 2005, **44**, 9684–9689.
29 J. Haisma, P. H. Joosten, H. J. P. Nabben, T. J. A. Popma and H. A. M. Van Hal, *Method of Providing Magnesium Fluoride Layers*, *US Pat.*, US4492721 A, 1985.
30 H. Li, P. Balaya and J. Maier, *J. Electrochem. Soc.*, 2004, **151**, A1878–A1885.
31 Y. Zhou, W. Liu, M. Xue, L. Yu, C. Wu, X. Wu and Z. Fu, *Electrochem. Solid-State Lett.*, 2006, **9**, A147–A150.

